CrossMark

Confirmation of Iron Emission Lines and Nondetection of TiO on the Dayside of KELT-9b with MAROON-X

David Kasper[1] , Jacob L. Bean[1] , Michael R. Line[2] , Andreas Seifahrt[1] , Julian Stürmer[3] , Lorenzo Pino[4] ,
Jean-Michel Désert[5], and Matteo Brogi[6,7,8]

[1] Department of Astronomy & Astrophysics, University of Chicago, 5640 South Ellis Avenue, Chicago, IL 60637, USA; kasperd@uchicago.edu
[2] School of Earth and Space Exploration, Arizona State University, Tempe, AZ 85281, USA
[3] Landessternwarte, Zentrum für Astronomie der Universität Heidelberg, Königstuhl 12, D-69117 Heidelberg, Germany
[4] INAF-Osservatorio Astrofisico di Arcetri, Largo Enrico Fermi 5, I-50125 Firenze, Italy
[5] Anton Pannekoek Institute for Astronomy, University of Amsterdam, 1098 XH Amsterdam, The Netherlands
[6] Department of Physics, University of Warwick, Coventry CV4 7AL, UK
[7] INAF-Osservatorio Astrofisico di Torino, Via Osservatorio 20, I-10025 Pino Torinese, Italy
[8] Centre for Exoplanets and Habitability, University of Warwick, Coventry CV4 7AL, UK

Abstract

We present dayside thermal emission observations of the hottest exoplanet KELT-9b using the new MAROON-X spectrograph. We detect atomic lines in emission with a signal-to-noise ratio of 10 using cross-correlation with binary masks. The detection of emission lines confirms the presence of a thermal inversion in KELT-9b's atmosphere. We also use M-dwarf stellar masks to search for TiO, which has recently been invoked to explain the unusual Hubble Space Telescope WFC3 spectrum of the planet. We find that the KELT-9b atmosphere is inconsistent with the M-dwarf masks. Furthermore, we use an atmospheric retrieval approach to place an upper limit on the TiO volume mixing ratio of $10^{-8.5}$ (at 99% confidence). This upper limit is inconsistent with the models used to match the WFC3 data, which require at least an order of magnitude more TiO, thus suggesting the need for an alternate explanation of the space-based data. Our retrieval results also strongly prefer an inverted temperature profile and atomic/ion abundances largely consistent with the expectations for a solar composition gas in thermochemical equilibrium. The exception is the retrieved abundance of Fe^{+}, which is about 1–2 orders of magnitude greater than predictions. These results highlight the growing power of high-resolution spectrographs on large ground-based telescopes to characterize exoplanet atmospheres when used in combination with new retrieval techniques.

1. Introduction

Since its discovery just a few years ago, the ultrahot-Jupiter KELT-9b has become a touchstone for studying the extreme physics and chemistry in the atmospheres of highly irradiated planets (Gaudi et al. 2017). The key observational results to date for the atmosphere of this planet include the detection of a wide range of neutral and ionized atomic species (Hoeijmakers et al. 2018, 2019; Cauley et al. 2019; Yan et al. 2019; Pino et al. 2020; Turner et al. 2020), an extended envelope of excited hydrogen (Yan & Henning 2018), dynamics and variability (Cauley et al. 2019), and heat transport from H_2 dissociation and recombination (Mansfield et al. 2020; Wong et al. 2020). The overall picture that is painted by these observations is consistent with the predictions of models that assume roughly solar composition, thermochemical equilibrium, and standard atmospheric physics (Bell & Cowan 2018; Kitzmann et al. 2018; Lothringer et al. 2018; Parmentier et al. 2018; Tan & Komacek 2019; Fossati et al. 2021). This broad brushstroke agreement is a major success of exoplanet atmosphere theory, and it enables using the data and models together to explore the detailed properties of KELT-9b's atmosphere.

Despite most observations of KELT-9b agreeing with established atmospheric models, recent measurements of the planet's dayside thermal emission defy expectations. Changeat & Edwards (2021) used Hubble Space Telescope (HST) WFC3 data to show that the planet's low-resolution thermal emission spectrum in the near-infrared is highly featured. They suggested that these features could be explained by opacity from the molecules TiO, VO, and FeH. The presence of molecules on the dayside of the planet is surprising because the infrared photospheric temperature has been measured to be ~4500 K (Mansfield et al. 2020; Wong et al. 2020) and molecules should be dissociated at these high temperatures (Kitzmann et al. 2018; Lothringer et al. 2018). Changeat & Edwards (2021) point out that their derived molecular abundances are many orders of magnitude greater than what is predicted by thermochemical equilibrium. Therefore, these results would likely require a high-metallicity composition and/or nonequilibrium chemistry, which would be novel results for ultrahot-Jupiter atmospheres.

We present ground-based high-resolution observations of the dayside emission from KELT-9b that were obtained using the new MAROON-X instrument on the Gemini-North telescope (Seifahrt et al. 2016, 2018, 2020). We analyzed these data to test the claimed detection of molecules by Changeat & Edwards (2021) and to further explore the chemistry of this unique planet. MAROON-X's red optical bandpass was designed to cover the rich molecular spectra of M-dwarf stars for extreme-precision radial-velocity measurements. The

Table 1
Log of Observations

UT Date	Exposures	Planet Phase Range	Airmass	Conditions	Seeing	Average Blue Arm S/N
2020 May 28 12:15 → 14:55	37	0.383 → 0.458	1.21 → 1.07	some passing clouds	0."5 to 0."8	140
2020 May 31 10:15 → 14:07	53	0.353 → 0.461	1.70 → 1.10	clear	0."3 to 0."5	200
2020 June 03 10:18 → 12:53	36	0.379 → 0.444	1.60 → 1.12	light clouds early	0."4 to 0."6	191

spectra of M dwarfs in this wavelength range are dominated by the same molecules that are suggested by the WFC3 data, so the instrument is ideally suited for this investigation.

We present our observations in Section 2. We describe two analyses of the data in Sections 3 and 4 that yield the detection of the planet's atmosphere and constraints on its properties. We conclude with a discussion of the results in Section 5.

2. Observations

We used MAROON-X to obtain 5.9 hr of data (7.7 hr total observing time including overheads) during pre-secondary eclipse phases of KELT-9b over three nights in 2020 May and June with both the "blue" (500–663 nm) and "red" (654–920 nm) channels. This was the first regular observing run of the instrument following commissioning and science verification in 2019. The two MAROON-X detectors read out at different rates, so we used different exposure times to maintain a constant cadence throughout the observations (blue channel: 200 s, red channel: 180 s). We also continued observing past the start of the secondary eclipse during two of the nights to obtain data when the planet was not visible as a control (1.1 hr open-shutter time, 1.25 hr total observing time including overhead). Table 1 gives a log of the observations.

3. Detection of the Planet's Atmosphere

We performed two analyses of our data to characterize KELT-9b's atmosphere. The first analysis used a cross-correlation function (CCF) technique with line-weighted binary templates. We broadly followed the Pino et al. (2020) Appendices A & B approach to create a time (i.e., phase) evolving spectrum containing planet lines normalized to the planet plus star continuum.

We used nine stellar templates as masks for the CCF analysis. These masks correspond to F9, G2, K2, K6, M0, M2, M3, M4, and M5 stellar types and come from the ESPRESSO data reduction pipeline ("ESPRESSO DRS"[9]). The masks span the transition from ionized and neutral atoms to molecules as the dominant species in hydrogen-dominated atmospheres and are typically considered as plausible proxies for hot Jupiters. These masks were built from observed stellar spectra (e.g., Suárez Mascareño et al. 2020). Therefore, they should not suffer from errors in line positions and strengths that sometimes hinder the use of theoretical templates, which has been a particular problem for searches for TiO (Hoeijmakers et al. 2015; Nugroho et al. 2017; Herman et al. 2020; Serindag et al. 2021). The M-dwarf masks also contain lines from VO, which is another molecule that was proposed by Changeat & Edwards (2021).

For this analysis, we calculate the detection signal-to-noise ratio (S/N) in our CCF maps by normalizing the peak value with the mean and standard deviation of the values in the rest of
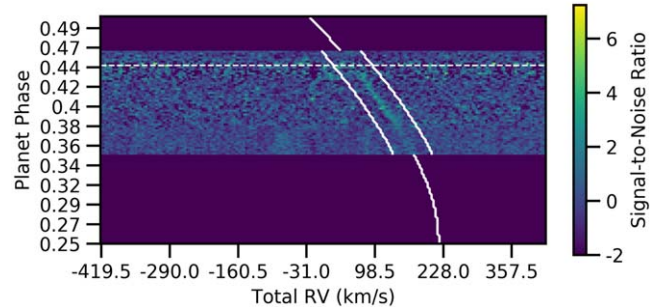

Figure 1. S/N of the planetary atmospheric signal with the G2 stellar template. This data set is the coaddition of the three nights of observations using the MAROON-X blue channel. The data series were coadded by nearest phase matching to the May 31 night as that data set contained the complete phase ranges of the other two nights. This procedure gave minimal signal smearing caused by a maximum phase mismatch of 0.1% (i.e., 130 s). The color quantifies the number of standard deviations from the mean response within the phases observed (with additional, nonobserved phases shown as zero S/N for clarity). The horizontal white dashed line indicates the beginning (i.e., first contact) of the secondary eclipse as calculated from the most recent ephemeris (phase 0.4449; Mansfield et al. 2020; Wong et al. 2020). The white solid lines indicate the predicted trace of the planetary atmosphere in planet+system velocity with a ± 10 km s^{-1} offset applied during the observed phases.

the map after applying an iterative 3σ clipping. We confirm that this approach gives similar (but slightly higher) detection S/N as the Welch's T-test that was developed for CCF analyses by Brogi et al. (2013).

As shown in Figure 1, the CCF exposure matrix of the combined data series demonstrates that the planet's atmosphere is detected at high confidence along the expected radial-velocity trace of the planet. The signal disappears at secondary eclipse when the planet is blocked by the star. The relatively weaker signal strength along the trace at the earliest observed phases is due to these phases only being covered by one of our three data sets. Nevertheless, even here the strength of the detection is high (compare to Figure 2 in Pino et al. 2020). As previously discovered by Pino et al. (2020), we see a positive correlation between the masks and the data, which indicates that the spectral lines are in emission due to a thermal inversion in the planet's dayside atmosphere.

Figure 2 shows the detection S/N as a function of mask spectral type for the blue and red channel data. All of the high-S/N detections were found near the expected planet and system velocities, which points to the nature of the recovered signal as planetary in origin. This plot demonstrates the relative importance of the signal in the blue channel over the red channel in the confidence of detection despite very similar data quality (photon-limited S/N within 2%) in the two channels. The earlier spectral-type masks give detection confidences approaching 10σ in the blue channel. The M-type masks give substantially lower detection confidences in the blue channel, and do not yield a significant detection in the red channel. These results suggest that KELT-9b's dayside spectrum is dominated by the atomic lines (primarily neutral iron; see
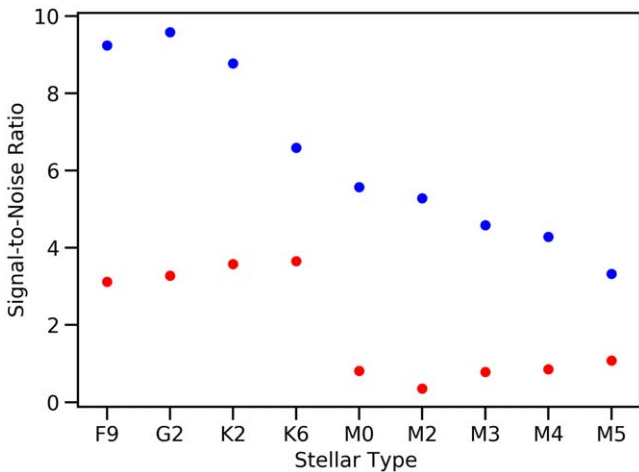
Figure 2. Detection S/N of the planetary atmospheric signal as a function of template stellar type. The peak S/N for the coaddition of the three observation sequences are shown for each arm independently. The absolute peak in S/N (at 9.6σ) occurs in the blue channel (blue points), utilizing the G2 mask. The blue channel broadly has an inverse relationship between signal strength and later spectral type. The red channel (red points) has a marginally significant response at early spectral types and is indistinguishable from noise at later spectral types.

Section 4) that are more prevalent in the earlier-type masks and that are concentrated in the bluer part of the MAROON-X bandpass. The lack of a significant detection with the M-type masks in the red channel disfavors the presence of molecules like TiO.

4. Retrieval Analysis

In our second analysis we applied the Brogi & Line (2019) cross-correlation retrieval framework to derive abundances and the vertical temperature structure of KELT-9b's atmosphere. We applied the retrieval approach to the three nights of data independently. We performed a "free" retrieval in that we did not enforce radiative–convective or thermochemical equilibrium. We closely followed the approach described in Brogi & Line (2019) and Line et al. (2021), except we use principle component analysis (PCA; de Kok et al. 2013; Pelletier et al. 2021) telluric/stellar removal procedure instead of the polynomial-fitting-based airmass detrending method. The following procedure is predicated on the assumption that the total signal can be written as

$$S(\lambda, t) = \left(1 + \frac{F_p(\lambda, t)}{F_\star(\lambda, t)}\right)\mathcal{T}(\lambda, t), \qquad (1)$$

where $F_p/F_\star$ is the secondary eclipse depth and $\mathcal{T}(\lambda, t)$ is a matrix that encapsulates the time- and wavelength-dependent instrumental throughput, telluric transmittance, and stellar spectrum (see Appendix A of Pino et al. 2020).

To briefly summarize the procedure for a given night of data: (1) a singular value decomposition is performed on the data cube for each order (frames/phases/time × pixel/wavelength) with the first N eigenvalues (we chose four, but the results are insensitive to the exact value) nulled to remove the dominant (nonplanetary) contributions to $\mathcal{T}(\lambda, t)$. The remaining eigenvalues/vectors are then used to reconstruct the residual matrix that contains the planetary signal (see Section 2 of de Kok et al. 2013). (2) Independently, the top N eigenvectors/values are used to reconstruct the $\mathcal{T}(\lambda, t)$ absent the true planetary signal. (3) A planetary and stellar model are used to produce an $F_p/F_\star$

spectrum. (4) The results of steps (2) and (3) are combined to create "model-injected" data (after the appropriate Doppler shift is applied to the model at each phase given the planetary, K_p, and system+barycenter velocities, $V_{sys} + V_{bary}$), and (5) the PCA is applied to this model-injected data to produce a model-injected residual matrix (analogous to what is done to the data in step (1)). (6) The post-PCA residual matrices products from (1) and (5) are then cross-correlated and log-likelihood computed, frame by frame (spectrum by spectrum) within each order, over all orders and then summed, resulting in a single log-likelihood value for a given model spectrum and velocity pair. Steps (3)–(6) are then repeated within a Bayesian parameter estimation tool at each iteration (PyMultiNest; Feroz & Hobson 2008). See Brogi & Line (2019) and Pelletier et al. (2021) for more details on this analysis/retrieval procedure. The retrieval analysis is performed on the blue and red arm data simultaneously and took 5 days to run for each data series.

The forward model used to generate the planetary spectrum utilizes the three-parameter Guillot (2010) and Line et al. (2013) temperature–pressure profile (TP) parameterization, uniform with altitude mixing ratios for H^-, Fe, Fe^+, Ti, Ti^+, Ca^+, Mg, and TiO, the planet Keplerian (K_p) and system velocities (V_{sys}), and a dilution/scale factor, a, for a total of 14 free parameters. We used the most recent "TOTO" line list for TiO (McKemmish et al. 2019), H bound–free opacities from John (1988), and the "Kurucz" atomic data available through the HELIOS-K package (Grimm & Heng 2015; Grimm et al. 2021). All cross sections (atomic/molecular) are generated with the HELIOS-K package assuming a $0.01\,cm^{-1}$ resolution ($R \sim 5$ million) and a $100\,cm^{-1}$ wing cutoff, over a grid of temperatures (12 points from 2000 to 4000 K) and pressures (18 points from μbar–300 bar). Cross sections are then downsampled through interpolation to a constant $R = 500\,k$. The core thermal emission radiative transfer was originally presented in Line et al. (2013), and more recently in Zalesky et al. (2019) and Line et al. (2021).

Figure 3 shows the results of the retrieval analysis. The results from looking at the three nights of data separately agree very well, and the planet and system velocities are found to match previous measurements. The derived TP profile quantifies the thermal inversion indicated by the analysis in Section 3. The confidence interval on the retrieved TP profile encompasses the prediction of a 1D radiative–convective equilibrium calculation (assuming a dayside irradiation temperature of 4600 K and a 10× solar metallicity) using the methods described in Arcangeli et al. (2018).

The derived abundances of H^-, Fe, Ti, Mg, and TiO are found to be in agreement with the expectations for a roughly solar composition gas in thermochemical equilibrium. The retrieval indicates a stringent upper limit on the abundance of TiO of $10^{-8.5}$ at 99% confidence, again consistent with no detection at the abundances proposed by Changeat & Edwards (2021).

The retrieved abundances of Fe^+, and to a lesser extent Ti^+ and Ca^+, are higher than expected. Our model assumes local thermodynamic equilibrium (LTE) to compute both the electron energy level populations of the absorbing gases (through the Boltzmann equation) and for predicting the partitioning of elements into different atoms, ions, and molecules for a given set of abundances (through the Saha equation). Photoionization, which is a non-LTE process, is
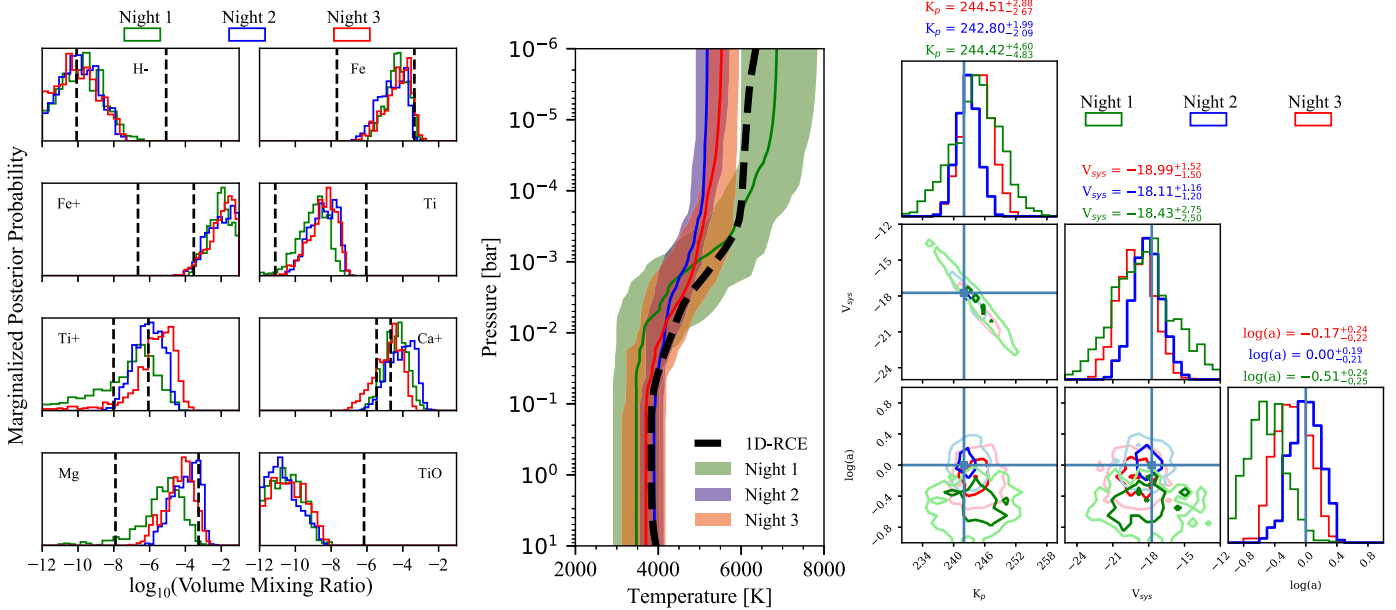
Figure 3. Retrieval results for KELT-9b. The left panels show the volume mixing ratios for key chemical species. The vertical dashed lines represent the range of abundances encountered in chemical equilibrium along the temperature profile for a $10\times$ solar metallicity atmosphere (Pino et al. 2020). The central panel shows the derived temperature–pressure profiles (colored lines and shaded 1σ confidence regions) along with the prediction from a 1D radiative–convective equilibrium model (black dashed line). The right panels show the derived planet and system velocities (solid lines are predicted values from previous constraints) along with the logarithm of the dilution factor, which is expected to be centered on zero.

known to impact the abundances of Fe and Mg species at low pressures in KELT-9b's atmosphere (Fossati et al. 2021). However, the total number of neutral and ionized atoms for a given element derived from a free retrieval would still equal the overall abundance of that element if it were just a question of changing the ionization balance. In this case the total abundance of neutral and ionized Fe would imply a roughly $100\times$ solar metallicity, which we consider unlikely. Non-LTE may also impact the electron energy level populations, which would directly affect the radiative transfer calculations in our model, and thus is more difficult to account for.

Figure 4 shows the second night's data cross-correlated (as a function of K_p and V_{sys}) with the template spectrum randomly drawn from the retrieved posterior probability distribution. In the bottom panel we show the individual gas contributions along a slice in V_{sys} at the nominal K_p. We note that this representation, which relies upon only a single template model, of the planetary signal (and individual gas contributions) does not fully reflect all of the information available in the data. While a gas may be constrained within the retrieval itself, it may not necessarily show up as a strong signal in the CCF representation. The retrieval analysis measures the change in the relative log-likelihood per change in gas abundance, which takes into account all of the corresponding degeneracies, whereas a simple CCF slice cannot fully represent for this.

From these figures we see that neutral iron is driving the detection. Interestingly, the CCF peak position differs by a few km s^{-1} among the individual species. This is perhaps an indication that the species are distributed differently in the planet's atmospheres (i.e., they experience different effective velocities), thus contradicting our assumption of 1D geometry. The retrieval analysis maximizes the log-likelihood, which depends on the velocities and abundances of each gas. As such, the retrieval finds an average solution, but may not find the correct velocity pair for any individual gas itself. A similar, but larger, velocity offset was recently seen between Fe and TiO in
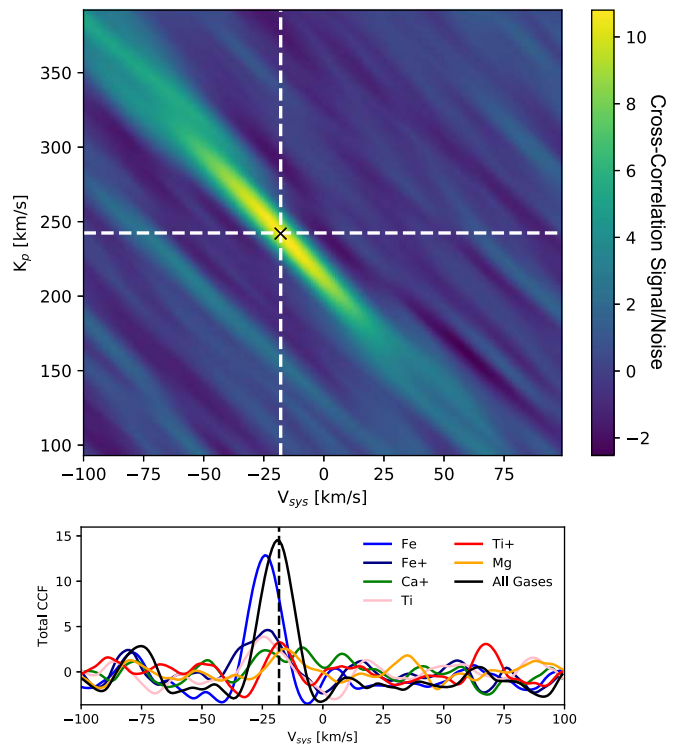

Figure 4. Cross-correlation S/N of the second night of data (May 31) with a randomly selected model drawn from the posterior as the template. We cross-correlate the template model with each K_p–V_{sys} pair to produce the top panel (e.g., Birkby 2018). The S/N is calculated by normalizing the CCF map in the same way that was done for the binary mask calculation. The bottom panel is a cross-cut in V_{sys} at the nominal $K_p = 242$ km s^{-1} to illustrate the contributions from each individual species. This is done by cross-correlating the same template model with all gases removed but one (and the H$^-$ continuum).

WASP-33b (which is a cooler planet than KELT-9b; Cont et al. 2021). If such an inhomogeneity exists in KELT-9b's atmosphere then that could provide another explanation for our surprising retrieval results for the ionized species. However, chemical inhomogeneities cannot explain the presence of TiO in the HST/WFC3 and the concomitant lack of a detection in our MAROON-X data because we do not see evidence of a TiO signal at any velocity consistent with a planetary origin.

5. Discussion

Our detection of atomic emission lines in the dayside spectrum of KELT-9b agrees with the previous results of Pino et al. (2020) that were obtained with HARPS-N. The larger aperture of the Gemini-N telescope yields higher signal-to-noise data and a stronger detection. The extended red optical coverage of MAROON-X permits a sensitive search for the molecules proposed by Changeat & Edwards (2021), particularly TiO. The TiO molecule has historically been challenging to detect in exoplanet atmospheres with high-resolution techniques due to problems with the line list. To maximize our chance of a detection, we used the latest line list for TiO in our retrieval analysis (see Section 4; McKemmish et al. 2019), and we used templates derived from the observed spectra of M dwarfs (see Section 3).

Our data strongly disfavor the high abundance of TiO that is needed to match the HST/WFC3 spectrum. We therefore see no evidence for molecules that could be due to nonequilibrium chemistry or a highly nonsolar abundance pattern. Instead, our data reinforce and extend the previous ground-based high-resolution studies that highlight the presence of atomic rather than molecular species in KELT-9b's atmosphere.

The origin of the discrepancy between the ground-based high-resolution results and the WFC3 data remains a mystery. WFC3 results have been seen as the gold standard for transit spectroscopy measurements over the past decade. However, features in spectra that have come from single WFC3 transit/eclipse observations, like the KELT-9b data set, have sometimes been overinterpreted in our opinion. Our own analysis of the WFC3 data for KELT-9b yields a spectrum that is different than the Changeat & Edwards (2021) spectrum because we account for the stellar pulsations that were discovered by Wong et al. (2020) and Mansfield et al. (2020) (B. Jacobs 2021, private communication). It remains to be seen whether this version of the WFC3 spectrum can be reconciled with the ground-based data. Ultimately, observations of KELT-9b's transmission, dayside emission, and phase curve with JWST would be very valuable for furthering our understanding this extreme planet.

With a mass of $\sim 3\,M_{\rm Jup}$, KELT-9b is not expected to have a particularly metal-enriched atmosphere if the mass–metallicity trend observed for the solar system giant planets is universal. Our retrieval results are largely consistent with this expectation. However, the derived abundance of Fe^+ is very high. We attribute this to the use of simplifying assumptions in the retrieval model (1D, constant abundances with altitude, LTE, etc.). Retrieval techniques for high-resolution studies of exoplanet atmospheres have advanced rapidly in the past few years (Brogi et al. 2017; Pino et al. 2018; Brogi & Line 2019; Shulyak et al. 2019; Gibson et al. 2020; Pelletier et al. 2021). The improvement in the data quality from new spectrographs on the largest ground-based telescopes, like MAROON-X on

Gemini-N, motivates further improvement in retrieval techniques to reveal exoplanet atmospheres in greater detail.

ORCID iDs

David Kasper ⬤ https://orcid.org/0000-0003-0534-6388
Jacob L. Bean ⬤ https://orcid.org/0000-0003-4733-6532
Michael R. Line ⬤ https://orcid.org/0000-0002-2338-476X
Andreas Seifahrt ⬤ https://orcid.org/0000-0003-4526-3747
Julian Stürmer ⬤ https://orcid.org/0000-0002-4410-4712
Lorenzo Pino ⬤ https://orcid.org/0000-0002-1321-8856
Matteo Brogi ⬤ https://orcid.org/0000-0002-7704-0153

References

Arcangeli, J., Désert, J.-M., Line, M. R., et al. 2018, ApJL, 855, L30
Astropy Collaboration, Price-Whelan, A. M., Sipőcz, B. M., et al. 2018, AJ, 156, 123
Bell, T. J., & Cowan, N. B. 2018, ApJL, 857, L20
Birkby, J. L. 2018, arXiv:1806.04617
Brogi, M., Line, M., Bean, J., Désert, J.-M., & Schwarz, H. 2017, ApJL, 839, L2
Brogi, M., & Line, M. R. 2019, AJ, 157, 114
Brogi, M., Snellen, I. A. G., de Kok, R. J., et al. 2013, ApJ, 767, 27
Cauley, P. W., Shkolnik, E. L., Ilyin, I., et al. 2019, AJ, 157, 69
Changeat, Q., & Edwards, B. 2021, ApJL, 907, L22
Cont, D., Yan, F., Reiners, A., et al. 2021, A&A, 651, A33
de Kok, R. J., Brogi, M., Snellen, I. A. G., et al. 2013, A&A, 554, A82
Feroz, F., & Hobson, M. P. 2008, MNRAS, 384, 449
Fossati, L., Young, M. E., Shulyak, D., et al. 2021, A&A, 653, A52
Gaudi, B. S., Stassun, K. G., Collins, K. A., et al. 2017, Natur, 546, 514
Gibson, N. P., Merritt, S., Nugroho, S. K., et al. 2020, MNRAS, 493, 2215
Grimm, S. L., & Heng, K. 2015, ApJ, 808, 182
Grimm, S. L., Malik, M., Kitzmann, D., et al. 2021, ApJS, 253, 30
Guillot, T. 2010, A&A, 520, A27
Harris, C. R., Millman, K. J., van der Walt, S. J., et al. 2020, Natur, 585, 357
Herman, M. K., de Mooij, E. J. W., Jayawardhana, R., & Brogi, M. 2020, AJ, 160, 93
Hoeijmakers, H. J., de Kok, R. J., Snellen, I. A. G., et al. 2015, A&A, 575, A20
Hoeijmakers, H. J., Ehrenreich, D., Heng, K., et al. 2018, Natur, 560, 453
Hoeijmakers, H. J., Ehrenreich, D., Kitzmann, D., et al. 2019, A&A, 627, A165
Hunter, J. D. 2007, CSE, 9, 90
John, T. L. 1988, A&A, 193, 189
Kanodia, S., & Wright, J. 2018, RNAAS, 2, 4
Kitzmann, D., Heng, K., Rimmer, P. B., et al. 2018, ApJ, 863, 183
Line, M. R., Brogi, M., Bean, J. L., et al. 2021, Natur, 598, 580
Line, M. R., Wolf, A. S., Zhang, X., et al. 2013, ApJ, 775, 137
Lothringer, J. D., Barman, T., & Koskinen, T. 2018, ApJ, 866, 27
Mansfield, M., Bean, J. L., Stevenson, K. B., et al. 2020, ApJL, 888, L15
McKemmish, L. K., Masseron, T., Hoeijmakers, H. J., et al. 2019, MNRAS, 488, 2836
Nugroho, S. K., Kawahara, H., Masuda, K., et al. 2017, AJ, 154, 221

Parmentier, V., Line, M. R., Bean, J. L., et al. 2018, A&A, 617, A110
Pelletier, S., Benneke, B., Darveau-Bernier, A., et al. 2021, AJ, 162, 73
Pino, L., Désert, J.-M., Brogi, M., et al. 2020, ApJL, 894, L27
Pino, L., Ehrenreich, D., Wyttenbach, A., et al. 2018, A&A, 612, A53
Seifahrt, A., Bean, J. L., Stürmer, J., et al. 2016, Proc. SPIE, 9908, 990818
Seifahrt, A., Bean, J. L., Stürmer, J., et al. 2020, Proc. SPIE, 11447, 114471F
Seifahrt, A., Stürmer, J., Bean, J. L., & Schwab, C. 2018, Proc. SPIE, 10702, 107026D
Serindag, D. B., Nugroho, S. K., Mollière, P., et al. 2021, A&A, 645, A90
Shulyak, D., Rengel, M., Reiners, A., Seemann, U., & Yan, F. 2019, A&A, 629, A109

Suárez Mascareño, A., Faria, J. P., Figueira, P., et al. 2020, A&A, 639, A77
Tan, X., & Komacek, T. D. 2019, ApJ, 886, 26
Turner, J. D., de Mooij, E. J. W., Jayawardhana, R., et al. 2020, ApJL, 888, L13
Van Rossum, G., & Drake, F. L. 2009, Python 3 Reference Manual (Scotts Valley, CA: CreateSpace)
Virtanen, P., Gommers, R., Oliphant, T. E., et al. 2020, Nat. Methods, 17, 261
Wong, I., Shporer, A., Kitzmann, D., et al. 2020, AJ, 160, 88
Yan, F., Casasayas-Barris, N., Molaverdikhani, K., et al. 2019, A&A, 632, A69
Yan, F., & Henning, T. 2018, NatAs, 2, 714
Zalesky, J. A., Line, M. R., Schneider, A. C., & Patience, J. 2019, ApJ, 877, 24